1997 HST Calibration Workshop
Space Telescope Science Institute, 1997
S. Casertano, et al., eds.

The On-Orbit Performance of the STIS Detectors[1]

Randy A. Kimble[2]

Laboratory for Astronomy and Solar Physics, Goddard Space Flight Center, Greenbelt, MD 20771

Abstract. The Space Telescope Imaging Spectrograph (STIS), successfully installed into the *Hubble Space Telescope* in February 1997, achieves its advances over the first-generation *HST* spectrographs primarily through the use of modern large-format, two-dimensional array detectors. The performance of the STIS detectors, two Multi-Anode Microchannel Arrays (MAMAs) and one CCD, has been evaluated on-orbit as part of the Servicing Mission Orbital Verification (SMOV) program. All three detectors are functioning well. We report highlights of the results to date here.

1. Introduction

The Space Telescope Imaging Spectrograph is a versatile spectrograph covering the 115-1000 nm wavelength range in a variety of spectroscopic and imaging modes. (See Woodgate et al. [1992,1998] and the STScI *STIS Instrument Handbook* [Baum et al. 1996] for overviews of the STIS design and operations.) The principal advances offered by STIS stem primarily from the use of large-format two-dimensional array detectors. Two photon-counting Multi-Anode Microchannel Array (MAMA) detectors, each read out in a 2048 × 2048 format, record UV light, and one 1024 × 1024 pixel CCD covers the visible. Compared with the 1 × 512 element linear array detectors employed by the first-generation *HST* spectrographs, these two-dimensional array detectors enable STIS to provide observing modes with large spatial and/or spectral multiplexing gains.

The observing modes of STIS divide its wavelength range into four spectral bands. Figure 1 presents the quantum efficiency of the flight detectors and demonstrates how they combine to cover the instrument's observing range and also how their overlapping sensitivities provide a degree of redundancy. Band 1 (115-170 nm) is covered by a MAMA detector designated as the FUV MAMA, fabricated with an opaque CsI photocathode deposited directly on the front of its single curved-channel microchannel plate (C-plate). Band 2 (165-310 nm) is covered by a similar detector, the NUV MAMA, which utilizes a semi-transparent CsTe photocathode on the inside of the detector window. This detector provides additional coverage down to 115 nm in imaging and prism modes, and it serves as a backup to the FUV MAMA. The MAMAs were developed by Ball Aerospace and are both permanently sealed tubes with MgF_2 entrance windows. See Timothy (1994) and Joseph et al. (1995) for further details about the MAMA design and performance.

Each MAMA detector incorporates a 1024 × 1024 element anode array, but the processing electronics centroid event positions to half the spacing of the anode array, providing improved image sampling and higher resolution (but with larger flat-field variations) in a

[1]The results reported here represent the efforts of many people, including the STIS Investigation Definition Team and personnel of the Goddard Space Flight Center, Ball Aerospace, and the Space Telescope Science Institute.

[2]Co-Investigator, STIS Investigation Definition Team

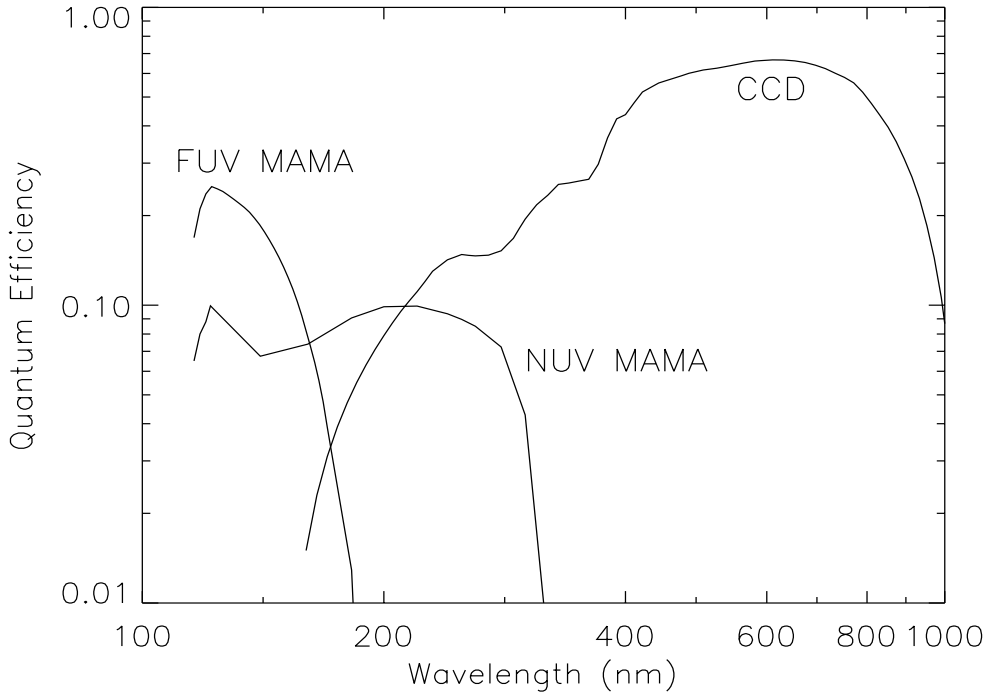

Figure 1. Quantum Efficiency of the STIS Flight Detectors

2048 × 2048 image format (Kasle & Morgan 1991). For historical reasons, this is referred to as the high resolution mode; all generic references to MAMA pixels in this paper (and in most other STIS documentation) refer instead to low-resolution pixels in the 1024 × 1024 format.

Bands 3 and 4 (305-555 nm; 550-1000 nm) are covered by a backside-thinned, UV-enhanced, multi-pinned-phase, 1024 × 1024 pixel CCD developed by Scientific Imaging Technologies (SITe). The CCD also provides backup to the NUV MAMA in the 180-305 nm range. The CCD is cooled to an operating temperature of -83 C using a four-stage thermoelectric cooler (TEC). The CCD and TEC are enclosed within a sealed, evacuated housing whose fused silica window is only slightly cooler than the rest of the instrument, minimizing the condensation of contaminants which could otherwise be deposited directly onto the much colder CCD. See Kimble et al. (1994) for a more comprehensive discussion of the CCD subsystem.

Since launch, a variety of performance and characterization tests have been carried out for STIS as part of the Servicing Mission Orbital Verification (SMOV) program. We report here on the highlights of the detector-related aspects of the SMOV program. For critical parameters that have not yet been or can not be measured directly in flight, we also cite relevant results from the pre-flight calibration.

2. CCD Performance

The 1024 × 1024 pixel STIS CCD is a backside-illuminated three-phase device, with 21 μm pixels, multi-pinned-phase implants and operation, and an enhanced UV response. The backside UV-enhancement process was developed by SITe for the STIS program. The resulting quantum efficiency (Figure 1) is stable, does not show QE hysteresis, and does not require a UV flood.

The CCD is fabricated with a readout amplifier in each of the four corners. There is an independent analog signal processing chain for each amplifier, and the STIS flight software supports full-frame, on-chip-binned, or subarray readout with any of the four amplifiers, as well as two and four amplifier readout modes. Initial functional testing on orbit verified that all four amplifier chains were functioning nominally. Observations since that first checkout have been carried out exclusively with the lowest noise amplifier, which was most fully characterized in ground testing. The redundant amplifiers are available as future backups.

Four commandable gain settings are available for the CCD. The noise performance *measured in flight* and the dynamic range for each setting are summarized in Table 1. Rough gain measurements made in flight are consistent with the more precisely determined ground values shown in the table. Two gain settings are recommended for general use: gain=1 for the greatest sensitivity to faint targets and gain=4 for the highest dynamic range and full well.

Table 1. CCD Noise/Dynamic Range.

Nominal Gain e/DN	Measured Gain e/DN	Noise (rms) *In-flight data*	Linear Range At 1% Rolloff	Single Frame Dynamic Range = Linear Range/Noise
1	0.995	4.0 DN = 4.0 e	33,000 e	8,250
2	2.01	2.7 DN = 5.4 e	86,000 e	16,000
4	4.11	1.7 DN = 7.0 e	144,000 e	20,600
8	8.38	1.3 DN = 10.9 e	144,000 e	13,200

In-flight mean bias levels vary over roughly 10 DN (data numbers in the 16-bit digitized readout) at gain=1 and 3 DN at gain=4 (due to temperature variations in the CCD and processing electronics); however, the *shape* of the bias frames is constant to <0.2 DN, so the bias level is well determined by the serial and parallel overscan data read out with each CCD frame. Under logarithmic stretch, some frames, particularly at gain=4, show "herringbone" noise that can be discerned by the eye. This pattern is low amplitude, however, <1 DN, and does not significantly affect the overall noise statistics in the image.

Charge transfer efficiency (CTE) was measured by both x-ray and edge response techniques in ground calibration, with parallel CTE results of 0.999994 @ 1620 e (x-ray) and 0.999991 @ 200 e, 0.99996 @ 10 e (edge response). Serial CTE's are higher. Additional ground calibration tests measured the parallel CTE performance under "sparse field" illumination, i.e. as would be encountered when observing the spectrum of a point source or an image of a dilute stellar field with only one or two stars per CCD column. These tests implied a charge loss up to 1.1% from the top of the CCD column to the bottom, for signal levels of 500 e/pixel, operating at the gain=1 voltage settings. For higher signal levels or the gain=4 voltage settings, the derived charge loss across the CCD is lower.

The x-ray CTE measurements can not be duplicated in flight, and the sparse field measurements have not yet been. However, edge response measurements (using onboard flat-field lamps for illumination) show no significant changes from ground measurements.

The median dark current at the CCD operating temperature of -83 C is only ∼0.0015 electrons/pixel/second, or 5-6 electrons/pixel/hour. Unless significant on-chip binning is employed, the noise from the median dark current is thus negligible compared with the read noise of the system. Of much greater significance are the effects of cosmic rays and radiation-induced hot pixels. With regard to these issues, the performance of the STIS CCD is very similar to that of WFPC2.

The cosmic ray rate observed on the STIS CCD outside of the South Atlantic Anomaly (SAA) is ∼1 event/cm^2/second. Roughly 30-40 pixels/second are affected at greater than a 20 electron level. Cosmic rays are most effectively removed from science data by specifying CR-SPLIT exposures to obtain multiple images from which cosmic rays can be vetoed.

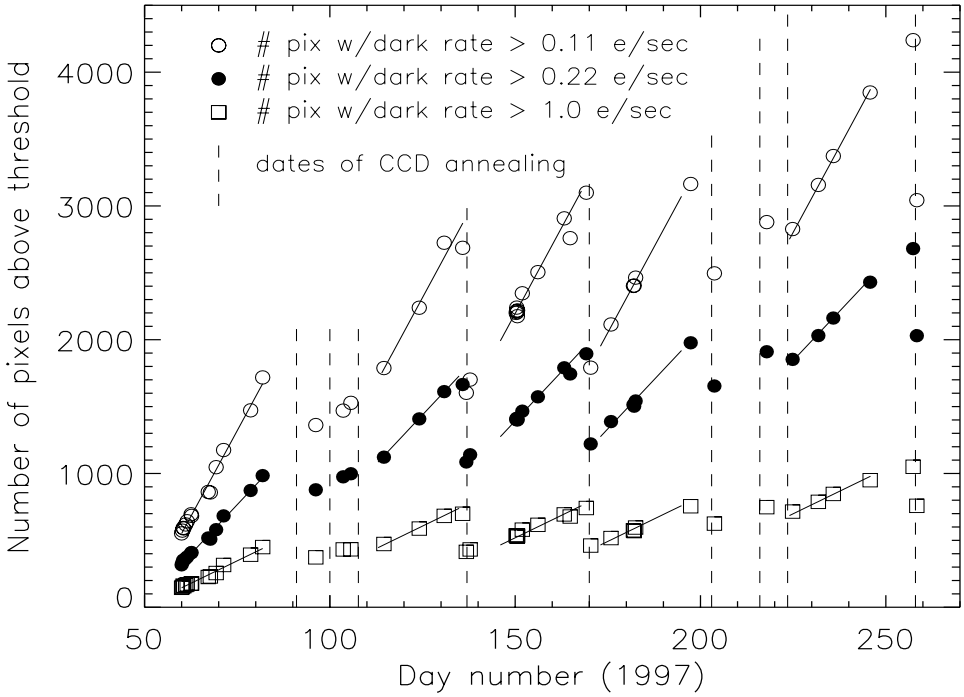

Figure 2. Growth of CCD Hot Pixels in Orbit

As expected for a CCD in space, energetic particle impacts on the STIS CCD produce "hot pixels" with enhanced dark current. As for WFPC2, warming of the CCD by turning off the thermoelectric cooler is effective at "annealing" some portion of the hot pixels. The STIS CCD reaches -5 C with the TEC off; annealing at this temperature for 12 hours is scheduled monthly. WFPC2 experience suggests that eventually a near steady state is reached in which the number of new hot pixels each month is similar to the number of old hot pixels that "heal" through the annealing process or spontaneously while the CCD is cold; hence the *net* growth rate of hot pixels over several years on orbit for WFPC2 is <8% of the instantaneous growth rate (Biretta et al. 1996). After the first few STIS annealing cycles, the net growth rate of hot pixels is down to about 30% of the instantaneous growth rate (see Figure 2); this fraction is expected to decrease as the hot pixel count asymptotically approaches a steady state. CCD dark frames are taken frequently to permit flagging of hot pixels in nearby science exposures. The most effective removal of hot pixels from science data can be accomplished by dithering the pointing between exposures to permit hot pixel vetoing. Additional details regarding the hot pixels and annealing behavior are reported in this volume by Beck & Landsman (1997).

An unpleasant feature of the SITe backside-illuminated devices, discovered during STIS ground testing, is a significant degradation of the CCD point spread function (PSF) at long wavelengths. While the core of the PSF remains sharp at all wavelengths, a substantial halo is seen at wavelengths longer than ∼750 nm, where the CCD silicon begins to become transparent. As an increasing fraction of the incident light reaches the substrate of the backside-illuminated device, scattering in the (unfortunately translucent) substrate material produces an ever larger halo, containing an increasing proportion of the overall energy (see Figure 3). At the longest wavelengths (1000 nm), the halo extends to hundreds of pixels in radius and contains up to ∼40% of the light, though each pixel in the halo of course captures a very small fraction of the peak brightness. This portion of the raw QE of the CCD is

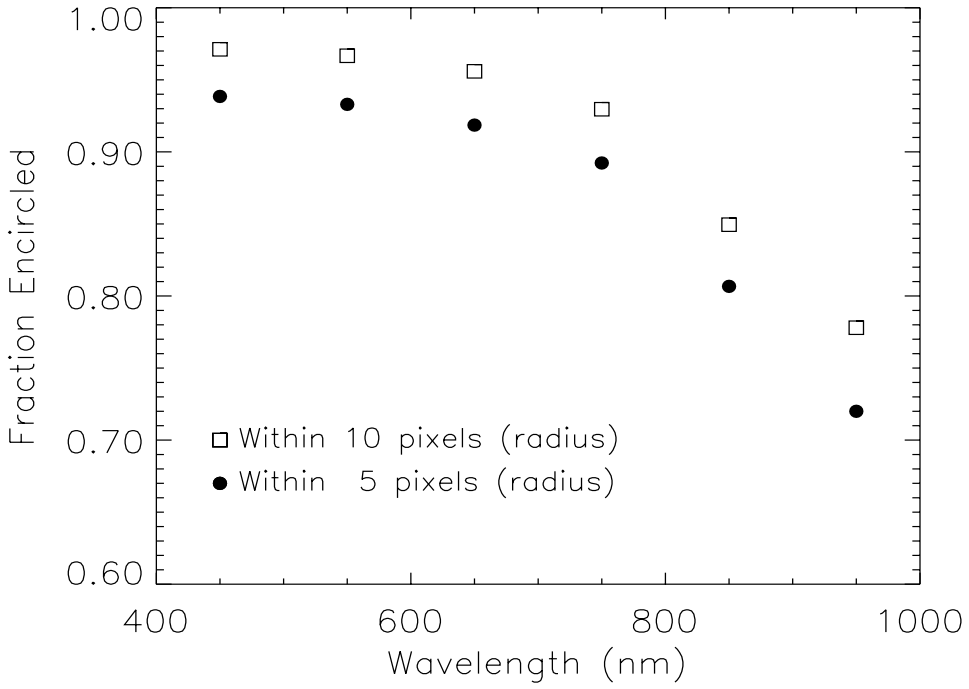

Figure 3. Encircled Energy vs. Wavelength and Extraction Radius for the STIS CCD

thus not useful, as it is not included within practical extraction radii for spectroscopy or imaging. The effect is stable over time, however, and can be appropriately calibrated.

The pixel-to-pixel flat-field behavior of the STIS CCD is also extremely stable. Short term (several hour) pixel-to-pixel stability at better than 0.1% rms was verified over several wavelengths spanning the CCD range in ground testing. In flight, broad-band flat-field exposures spanning a month constrain any changes in the pixel-to-pixel response to be <0.2% rms, and some portion of that variation is attributable to poorly removed hot pixels. Flats constructed using the onboard tungsten continuum lamps thus in general provide high S/N rectification of STIS CCD data.

The most significant issue affecting flat-fielding of STIS CCD data is fringing at the longer wavelengths (where the silicon begins to become transparent), caused by interference between the incident beam and light reflected by the substrate of the device. The fringing is negligible shortward of ∼750 nm, but grows to peak-to-peak amplitudes of 25 and 32% at 980 nm for G750L and G750M, respectively.

Rectification of the fringing pattern should be a tractable problem, because the behavior is completely stable with time. However, small shifts in the wavelength mapping onto the detector, caused by grating wheel non-repeatability and thermal drifts, do cause the fringe pattern to shift from exposure to exposure. Therefore, for accurate fringe removal, it is necessary to take contemporaneous spectral flats using the onboard tungsten lamps (at least until a suitable library of flats can be constructed); see Plait & Bohlin (1997) in this volume. Fortunately, the onboard lamps are bright, so the required exposures are short.

The spatial extent of the source along the slit is also an issue in fringe removal. Because of the PSF halo at long wavelengths, an extended source produces a smooth pedestal beneath the fringing modulation that is not present for a point source. However, a judicious combination of short and long-slit flats should serve. In data taken to date, Goudfrooij, Baum, & Walsh (1997, this volume) have successfully removed the fringes to better than

1% to ∼950 nm for a white dwarf spectrum using a short slit flat and for the extended source Io using a long-slit flat. Development of a systematic fringe removal methodology is a key goal of the in-flight calibration program.

Note that STIS imaging is generally unaffected by the fringing, because no narrow-band filters are used at long wavelengths, and the sky background is continuum zodiacal light, not airglow emission lines (as on the ground). Broadband continuum input smooths over the fringes completely; only a highly monochromatic long wavelength emission-line source would show fringe modulation in imaging mode.

3. MAMA Performance

The STIS MAMA detectors began on-orbit operations in late April 1997. Their use was delayed until software and scheduling changes had been made to deal with an unexpected issue of control electronics resets (see Section 4.) Since that time, the MAMA detectors have been performing very well. See Figures 3 and 4 for examples of FUV MAMA echelle spectroscopy and NUV MAMA imaging.

A few key MAMA performance parameters are shown in Table 2. Most of these data are from ground calibration, except for the dark rate, for which in-flight values are shown. While detector-only PSF and quantum efficiency can not be measured directly in flight, the end-to-end STIS performance indicates that the detector resolution and efficiency are nominal.

Table 2. Key MAMA Performance Parameters

	FUV MAMA	NUV MAMA
Wavelength Range	115 - 170 nm	165-310 prime 115 - 170 backup
Low-res Pixel Size	25 μm × 25 μm	25 μm × 25 μm
Spatial Resolution (FWHM)		
(w/hi-res readout)	22.7 μm	29.3 μm
Quantum Efficiency	∼21% (142 nm)	∼9.5% (237 nm)
Dark Rate	5-10 × 10^{-6} cts/pix/s*	0.6-1.5 × 10^{-3} cts/pix/s*
Dynamic Range (10% rolloff)		
Local (MCP limited)	220 cts/pixel/s*	340 cts/pixel/s*
Global (electronics limited)	305,000 cts/s	305,000 cts/s
Flat Field Uniformity		
(low-res pixels*)	6.4% rms	3.1% rms
Flat Field Stability	over 4 months	over 21 days
(changes in 2x2 pixels*)	<1% rms	<0.68% rms
Visible Light Rejection		
(QE at 400 nm)	1.5x10^{-10}	2.7x10^{-4}

*Note: "Pixel" refers to a low-resolution MAMA pixel here (*i.e.,* the 1024×1024 format).

A positive highlight of the in-flight performance is the extremely low background of the FUV MAMA, 5-10 times lower than the specification. The close agreement of the in-flight dark rate with that seen in ground test confirms the successful rejection of Cherenkov events produced in the detector window. Cherenkov photons produced by passage of energetic particles through the detector windows formed the dominant background in the Digicon detectors of the first-generation spectrographs; because the multiple Cherenkov photons produced by a particle transit are effectively simultaneous, they are rejected by the MAMA event processing logic.

The only performance disappointment with the MAMA detectors in flight is the high dark rate of the NUV MAMA. The specified dark rate for the tube was 1.25 × 10^{-4}

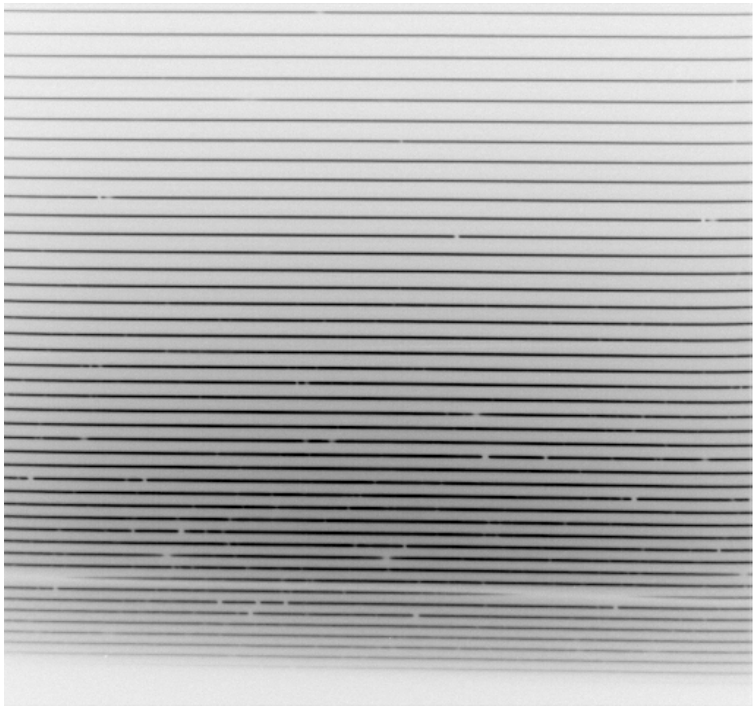

Figure 4. Echelle Spectrum (Mode E130M) of BD+28°4211 with the FUV MAMA. The spectrum shown covers 115-170 nm and shows broad Lyman α absorption (near the bottom) as well as numerous narrow stellar absorption features.

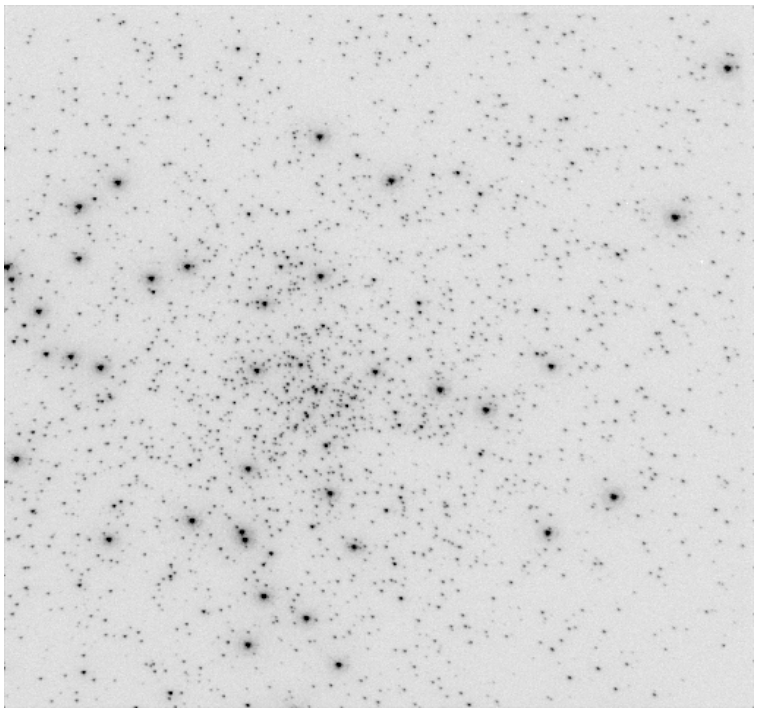

Figure 5. 270 nm Image of the Globular Cluster NGC6681 with the NUV MAMA. All of the features visible in the image are statistically significant detections of stars.

cts/second/pixel, and ground testing led us to expect substantial improvement over that specification in orbit. Unfortunately, in flight, energetic SAA particles excite meta-stable states in impurities in the window of the NUV MAMA; the subsequent phosphorescent decay produces UV photons that are detected by the MAMA photocathode. This phenomenon has long been recognized, and a screening program for phosphorescence was specifically instituted for the STIS detector windows; however, an error in the ground testing of this particular MgF_2 ingot allowed it to be used despite its poor phosphorescence characteristics.

The observed NUV MAMA background of 0.6-1.5 $\times$ 10^{-3} cts/second/pixel (the de-excitation rate varies with detector temperature) is roughly an order of magnitude higher than the specification. Over a typical 2000 second single-orbit exposure, the resulting dark count signal in a standard 2 $\times$ 11 pixel spectral extraction slit is 26-66 counts. Optimal extraction techniques or the use of a smaller extraction slit reduce the dark contribution below this level. Thus, in short exposure time observing programs, only very low S/N observations are significantly affected. However, long observations or those which are binned spectrally or spatially (such as for extended sources) can be significantly compromised by the unwanted background.

The high S/N potential of MAMA observing is a key issue; accordingly, a separate paper in this volume (Kaiser et al. 1997) is devoted entirely to this topic. Here we briefly summarize the extremely encouraging S/N results described in more detail in the Kaiser et al. paper.

Intrinsic pixel-to-pixel variations in the response of the MAMA detectors are significant: 3.9% and 2.8% rms for the FUV and NUV MAMA, respectively, in the 1024 $\times$ 1024 low-res pixel format (which supports the nominal resolution of all STIS modes). Severe odd-even effects in the high-res readout lead to much larger rms variations ($\sim$45-50%) in the 2048 $\times$ 2048 format. Nevertheless, high S/N MAMA observations are possible, particularly in spectroscopic modes, for two principal reasons: first, the flat-field behavior is extremely stable over time (as long as the instantaneous local count rate is not too high); second, the illumination pattern on the detector during an exposure provides a significant smoothing of the intrinsic response variations (especially in the high resolution echelle modes, where the Doppler effects of orbital motion shift the spectrum gradually over the detector format).

In first order spectroscopic modes, the raw detector response is smoothed over the cross-dispersion profile produced by the stellar spectrum. Convolving detector flat-field images with a Gaussian profile of two low-res pixels FWHM (representative of the cross-dispersion profiles in STIS spectroscopy) reduces the rms response variations to 2.5% (FUV) and 1.8% (NUV) per low-res pixel in the dispersion direction, and to 1.4% (FUV) and 0.92% (NUV) per two-pixel wide spectral resolution element. We would therefore expect the MAMAs to support point source spectroscopy up to S/N = 70 (FUV) and 110 (NUV) per resolution element *without applying a flat field calibration at all.* The additional smoothing produced by a typical Doppler amplitude of $\pm$8 high-res pixels in the high resolution echelle modes should increase the S/N capability to $\sim$140 (FUV) and $\sim$300 (NUV) per spectral resolution element, *again, without even using a flat.*

The S/N expectations without Doppler smoothing have been well confirmed in flight by SMOV observations in the low resolution first order modes G140L (FUV MAMA) and G230L (NUV MAMA). The extracted spectra of standard stars observed in these modes are compared with low order spline fits to various regions of the spectra. The rms fluctuations of the actual spectrum divided by the low order fit provide a measure of the S/N achieved. With the FUV MAMA, a spectrum with a count-statistic-limited S/N of 165 yielded an observed S/N of 80 with no flat field applied and 128 using a flat from ground testing. For the NUV MAMA, a spectrum with a count statistic potential of 200 yielded a S/N of 105 with no flat and 150 using a ground flat. Both results are in excellent agreement with predictions. See Kaiser et al. (1997) for details.

As this paper goes to press, preliminary results have just been reported from a STIS test of the "F-P split" technique previously employed to obtain very high S/N data with

the first generation *HST* spectrographs. In this technique, multiple spectra of the target are acquired, offset from each other in the dispersion direction, but overlying each other as closely as possible in the cross-dispersion direction. Iterative analysis of the resulting data then permits a simultaneous solution for the source spectrum and the flat-field response of the instrument. A preliminary analysis of MAMA echelle spectra taken in this manner (in STIS medium resolution echelle modes E140M and E230M) yields S/N of >250 per low-resolution pixel in the spectral direction (integrated over the cross-dispersion profile) and >350 per 2-pixel spectral resolution element. Details of the observations and analysis are presented by Gilliland et al. (1997) and Kaiser et al. (1997).

Thus, between the use of onboard calibration lamps to derive spectral flats, the smoothing effects of the illumination pattern and Doppler shifting, and the use of F-P split techniques, the MAMA detectors should routinely achieve the specified S/N performance of >100 per resolution element (when count statistics permit), and the ultimate S/N capability of STIS MAMA observations appears to be well beyond that level.

STIS also has the ability to perform time-resolved observing with the MAMA detectors, time-stamping the photons detected to an accuracy of 125 μsec for event rates below 30,000 cts/sec. The most rigorous test of this capability has been the acquisition of time-resolved spectra of the Crab pulsar with the NUV MAMA in mode G230L. The test was completely successful; see Lindler et al. (1997, this volume) for details.

4. Detector Electronics Resets

The biggest surprise encountered in operating STIS in flight has been the response of the detector control electronics to the radiation environment. Digital communication between the STIS control section microprocessor and the MAMA and CCD control electronics is optically coupled in order to eliminate conducted electrical noise and thereby maintain a low noise environment for the detectors. Unfortunately, the detector reset circuitry has been found to respond to transient spikes on the outputs of the optical isolators by partially resetting the detectors. These transients can be produced by the passage of trapped SAA particles or cosmic rays through the optical isolators. Though these components had been properly screened for total radiation dose effects, the transient response of the optical isolator reset-circuit combination was not recognized pre-flight.

In the CCD subsystem, the partial resets are relatively infrequent (roughly one per month of continuous operation) and are quite benign. A few CCD control voltages are set to non-functional but non-harmful values. By scheduling CCD voltage reconfiguration commands at each SAA exit or before CCD observation blocks, the chances of losing data from a CCD reset are rendered negligible.

The MAMA partial resets are both more frequent (approximately one per day per MAMA *if* the MAMA low voltage power is left on during SAA passages) and more complex. One effect of the partial reset is to turn off the detector high voltage abruptly. Though the detectors can withstand such shutdowns (as they must during the infrequent spacecraft safings), daily shutdowns of this type would be unnecessarily stressful to the high voltage system. In addition, when the partial reset occurs, there is a small but non-zero probability (1 in ~500) that a high voltage ramp-up to the full power supply rails could be spuriously commanded; this would very likely damage the MAMA tube if allowed to proceed. Once the reset phenomenon was recognized on orbit, the MAMA low voltage power was left off until protective software was installed onboard. This software monitors the MAMA subsystems on 40 msec timescales and is designed to intercept a reset-induced ramp-up before it can reach hazardous voltage levels.

In order to avoid potential stresses and risks to the MAMA detectors, they are now being operated in the following manner. The MAMA low voltage system is cycled off for each SAA crossing, but is powered on the rest of the time to maintain thermal stability

in the instrument. The MAMA high voltage, on the other hand, is ramped up and down at the nominal slow ramp rate once per day, in the block of contiguous non-SAA-crossing orbits, if the MAMA is scheduled for use that day. The MAMAs have been operated under this regimen for approximately 130 days. They have experienced seven resets outside of the SAA in that time. Hence, the best current estimate is that each MAMA will be shut down abruptly by a particle-induced reset approximately every three months (since the MAMA high voltage is on less than half of the time), and the spurious voltage ramp-up is unlikely ever to begin.

The principal effect of the resets, therefore, is to lower the available duty cycle for MAMA observations to about 40% of *HST* orbits. During the current period, when NICMOS observations are being accelerated to maximize its scientific yield before its cryogen is depleted, this duty cycle is more than adequate to schedule MAMA science. More complex, higher duty cycle operating schemes can be considered later if required.

5. Summary

The three STIS detectors have been evaluated through a variety of tests in the SMOV program. They are all functioning well. We expect them to support a rich scientific program in the coming years.

Acknowledgments. We are grateful to all whose efforts over many years made the development of STIS and the execution of the *HST* Second Servicing Mission so successful. The STIS IDT has been funded in response to NASA Announcement of Opportunity OSSA-4-84 through the *Hubble Space Telescope Project* at the Goddard Space Flight Center. This paper is based on observations with the NASA/ESA *Hubble Space Telescope*, obtained at the Space Telescope Science Institute, which is operated by AURA Inc. under NASA contract NAS5-26555.

References

Baum, S. et al. 1996, *STIS Instrument Handbook*, (Baltimore:STScI)

Beck, T., & Landsman, W. 1997, this volume

Biretta, J. et al. 1996, *WFPC2 Instrument Handbook*, (Baltimore:STScI)

Gilliland, R. L., et al. 1997, Instrument Science Report STIS, (Baltimore:STScI), in preparation

Goudfrooij, P., Baum, S. A., & Walsh, J. R. 1997, this volume

Joseph, C. L. et al. 1995, Proc. SPIE, 2551, 248

Kaiser, M. E., Lindler, D. J., Bohlin, R. C., & Gilliland, R. L. 1997, this volume

Kasle, D. B., & Morgan, J. S. 1991, Proc. SPIE, 1549, 52

Kimble, R. et al. 1994, Proc. SPIE, 2282, 169

Lindler, D. J., Gull, T. R., Kraemer, S. B., & Hulbert, S. J. 1997, this volume

Plait, P., & Bohlin, R. 1997, this volume

Timothy, J. G. 1994, Proc. SPIE, 2278, 134

Woodgate, B. et al. 1992, ESO Conf. and Workshop Proc. 44: Science with the Space Telescope, P. Benvenuti & E. Schreier, European Southern Observatory: Munich, 525

Woodgate, B. et al. 1998, in preparation